MOLINOS, M., NAVAS, P., MANZANAL, D. y PASTOR, M., 2021. Local Maximum Entropy Material Point Method applied to quasi-brittle fracture. Engineering fracture mechanics, vol. 241, ISSN 0013-7944. DOI 10.1016/j.engfracmech.2020.107394. Copyright Elsevier

Local Maximum Entropy Material Point Method applied to quasi-brittle fracture.

Miguel Molinos[a1], Pedro Navas[a2], Diego Manzanal[a], and Manuel Pastor[a]

[a] *ETSI Caminos, Canales y Puertos, Universidad Politéctnica de Madrid.*
c. Prof. Aranguren 3, 28040 Madrid, Spain

Abstract

This work aims to introduce an alternative technique to address the fracture process of brittle and quasi-brittle materials under the Material Point Method (MPM) framework. With this purpose the eigensoftening algorithm, developed originally for the Optimal Transportation Meshfree (OTM) approximation scheme, is extended to the MPM to present a suitable alternative to the existing fracture algorithms developed for such a methodology. The good fitting in the predictions made by the eigensoftening algorithm against both analytical and experimental results proves the excellent performance of the method when challenging applications are to model.

Keywords: Quasi brittle fracture, Local-*Max-Ent* approximation, Material Point Method, Solid Dynamics

---

1. Introduction

The failure mechanisms of quasi-brittle materials and the crack propagation have been studied from different fields such as materials science, structural engineering, earth science and petroleum engineering . The prediction of crack propagation has been approached with different numerical techniques. The Finite Element Method (FEM) is widely used in industrial application. However, the presence of cracks is a violation of the continuity requirement of the FEM. To overcome this issue, numerous numerical artifices have been proposed with the aim of reproducing such a complex behaviour. An example of this, is the gradual insertion of cohesive elements [1] at solid elements boundaries. To alleviate these shortcomings of the FEM, the Extended Finite Element Method (XFEM) in conjunction with level set

---

[1] Corresponding author: m.molinos@alumnos.upm.es
[2] Corresponding author: p.navas@upm.es

technique was introduced by Belytschko *et al.* [2] to handle arbitrary crack paths level set. Some relevant contributions to the XFEM are the modeling micro-scale crack propagation [3] or introducing a cohesive zone model [4].

The accurate and effective simulation of fracture propagation can be considered as one of the ongoing goals of the development of novel spatial discretisation methods like meshfree techniques. Some examples of it are the Material Point Method (MPM) [5, 6, 7], the Element-Free Galerkin Method (EFGM) [8, 9], the Smoothed Particle Hydrodynamics (SPH) [10, 11], the Optimal Transportation Meshfree (OTM) [12, 13] or Peridynamics [14, 15] among others.

Concerning MPM, fracture has been treated numerically through two different ways. One of these approaches is the CRAMP technique proposed by Nairn *et al.* [6]. The methodology removes the restriction of single-valued for the velocity field close to the crack. This is achieved through, at least, two sets of nodes. In this method, different labels are assigned to the material points and nodes to distinguish if they are in the same side of the crack or not. Under this approach, crack surface is described with line segments in 2D and triangle patches in 3D cases. In CRAMP, the chosen criteria for crack propagation relies on the energy release rate analysed by Tan & Nairn [16]. The second approach is to introduce failure material points to describe the evolution of the crack. In these methods, the formation of failed points describes the nucleation of cracks and its propagation and branching. Consequently, it is not necessary to state explicitly the position of the crack. This fact represents significant advantages over the CRAMP. Under this approach, the prediction of failure evolution is computed with a decohesion model. Further discussion about it can be found in Schreyer *et al.*[5] . Successful simulations are provided within the framework of the fracture of brittle materials by Chen *et al.* [17].

Similar to this approach, Schmidt *et al.* [18] introduced the concept of eigenfracture, where crack sets are approximated by means of eigen-deformations, which enable the material to develop displacement jumps at no cost of local elastic energy. Later, Pandolfi *et al.* [19, 12] proposed the eigenerosion approach to brittle fracture. In this technique, the concept of “erosion” of the material point is depicted, being the material point able to remain intact or become completely failed or eroded, when no loading capacity is bore. This method has been applied to simulate high complex phenomena such as dynamic fragmentation of metals [13] with good results. Recently, Zhang *et al.* [20] adopted the eigenerosion to resolve the dynamic fracture of brittle materials in the MPM framework. Nonetheless, the results exhibit an overestimation of tensile stress and strain peaks for quasi-brittle materials. Furthermore, this approach based on conventional MPM/GIMP has stress oscillations to solve.

To overcome the limitations observed in the EigenMPM, the present research proposes the eigensoftening algorithm developed by Navas *et al.* [21, 22] for the OTM framework and engineered for quasi-brittle materials. Inspired in the concept of the crack band model [23], since energy dissipation occurs through the softened (or failed) volume, this methodology can capture the gradual rather than abrupt dissipation of the fracture energy. Moreover, Molinos *et al.* [24] proposed a methodology to mitigate stress oscillations and deal with tensile instabilities. The traditional MPM technique is enhanced through the Local Maximum-Entropy (LME) approximation technique [25] for the spatial discretisation as well as a explicitly MPM Newmark Predictor-Corrector (NPC) scheme is derived for the time discretisation.

The paper is structured as follows. First meshfree methodology, eigenerosion and eigensoftening algorithms are presented in Section 2. Then, both approaches are compared and verified through comparisons with analytical and experimental results in Section 3. Finally, relevant conclusions are exposed in Section 4.

2. The meshfree methodology

This section aims to describe and introduce some non-standard techniques required to face the fracture problem under the MPM framework. In consequence, this section is structured as follows: first, in 2.1, the Newmark Predictor-Corrector (NPC) algorithm for the MPM will be exposed; next the LME approximants are introduced in 2.2 as an accurate alternative technique to interpolate data between particles and nodes, and finally fracture algorithms based on the eigendeformation concept are presented in 2.3.

2.1. The MPM time integration : A Newmark Predictor-Corrector scheme

The MPM [26] is a meshfree Lagrangian-Eulerian method where the continuum $\mathit{\Omega}$ is discretised with a finite set of material points (also known as particles in this research) $\hat{\Omega} = \{\vec{x}_p, p \in \mathcal{C}\} \subset \Omega$, where $\mathcal{C} = 1, \ldots, n_p$. Any particle field such as position, velocity, mass, stain and stress denoted by $\mathbf{x}$, $\mathbf{v}$, m, ε and σ, respectively, are assigned to each material point. In the present research, any particle quantity is denoted by $(\square_p)$. In addition to this set of material points, a set of fixed background nodes is introduced to compute the balance of momentum equation. This set of nodes is defined as

$\mathbf{X} = \{\vec{x}_I, I \in \mathcal{B}\} \subset \mathbb{R}^2$, where $\mathcal{B} = 1, \ldots, n_I$. In the present research, any nodal quantity is denoted by $(\square_I)$.

Since the MPM possesses the advantages of both Lagrangian and Eulerian descriptions, no element distortion takes place in the MPM. Therefore, it is an appropriate and efficient method to solve problems with moving discontinuities such as fracture evolution.

Without loosing generality, the MPM algorithm can be described with three main steps: (i) a variational recovery process, where particle data is projected to the grid nodes, (ii) an Eulerian step, where the balance of momentum equation is computed in the set of background nodes, finally (iii) a Lagrangian advection of the particles. In the present research, we adopted the explicit predictor-corrector time integration scheme proposed by Molinos *et al.* [24]. The purpose of this choice is motivated due to its proven robustness and stability for dynamic computations, Navas *et al.* [22]. In the first stage, the nodal velocity predictor $\vec{v}_I^{pred}$ is computed through particles velocities $\vec{v}_p$ and accelerations $\vec{a}_p$ and evaluated in the k time step,

$$\vec{v}_I^{pred} = \sum_{p\,\in\,\mathcal{C}} \frac{N_I(\vec{x}_p^k)\; m_p\; (\vec{v}_p^k + (1-\gamma)\;\Delta t\;\vec{a}_p^k)}{m_I}. \tag{1}$$

Where γ is an user-defined parameter (typically adopted as 0.5), $\mathbf{m}_I$ represents the lumped mass matrix, and $N_I(\vec{x}_p^k)$ is the nodal contribution of the shape function evaluated in the particle coordinates $\vec{x}_p^k$. This way of computing the nodal predictor is numerically stable as well as minimises the computational effort. Once nodal velocities are obtained, the essential boundary conditions are imposed. After that, an Eulerian phase is computed in the set of nodes in a FEM-like way, where nodal forces $\vec{f}_I^{k+1}$ are computed through the equilibrium equation. Next the nodal velocities are corrected in a *corrector* stage:

$$\vec{v}_I^{k+1} = \vec{v}_I^{pred} + \gamma\;\Delta t\;\frac{\vec{f}_I^{k+1}}{\mathbf{m}_I^{k+1}}\;. \tag{2}$$

Finally, in order to update the particles, those are advected in the Lagrangian stage as

$$\vec{a}_p^{k+1} = \sum_{I \, \in \, \mathcal{B}_p} \frac{N_I(\vec{x}_p^k) \; \vec{f}_I^k}{\mathbf{m}_I^k} \, , \tag{3}$$

$$\vec{v}_p^{k+1} = \vec{v}_p^n + \sum_{I \, \in \, \mathcal{B}_p} \Delta t \; \frac{N_I(\vec{x}_p^k) \; \vec{f}_I^k}{\mathbf{m}_I^k} \, , \tag{4}$$

$$\vec{x}_p^{k+1} = \vec{x}_p^n + \sum_{I \, \in \, \mathcal{B}_p} \Delta t \; N_I(\vec{x}_p^k) \; \vec{v}_I^k + \frac{1}{2}\Delta t^2 \; \frac{N_I(\vec{x}_p^k) \; \vec{f}_I^k}{\mathbf{m}_I^k} \, . \tag{5}$$

Appendix A summarises the complete pseudo-algorithm.

2.2. Spatial interpolation technique : Local Maximum-Entropy approximants

Local Maximum-Entropy (LME) approximation scheme was introduced by Arroyo & Ortiz (2006)[25] as a bridge between finite elements and meshfree methods. The basic idea of the shape functions based on such an estimate is to interpret the shape function $N_I(\vec{x})$ as a probability. This allows us to introduce two important limits: the principle of maximum-entropy (*max-ent*) statistical inference stated by Jaynes [27], and the Delaunay triangulation which ensures the minimal width of the shape function.

This approximation scheme represents an optimal compromise, in the sense of Pareto, between the *unbiased statistical inference* based on the nodal data which leads to the principle of *Maximum-Entropy* stated by Jaynes [27], and the definition of local shape functions of *least width* the least biased shape functions. Following [25], entropy of a discrete random variable can be defined as the uncertainty of the random variable. A measure of this uncertainty can be obtained by means of Shannon's entropy:

$$H(p_1, \ldots, p_n) = -\sum_{I=1}^{N_n} p_I \; \log p_I \tag{6}$$

where p_I stands for probability of the random variable outcomes. By interpreting these probabilities as the shape functions $N_I(\vec{x})$ of an approximation scheme, equation (6) can be regarded as a measure of the uncertainty of the approximation. To reach a compromise between two competing objectives, a Pareto set is defined as,

$$(\text{LME})_\beta \quad \text{For fixed } \vec{x} \text{ minimise } f_\beta(\vec{x}_p, N_I) := \beta U(\vec{x}_p, N_I) - H(N_I)$$

$$\text{subject to} \begin{cases} N_I \geq 0, \ \text{I=1, ..., n} \\ \sum_{I=1}^{N_n} N_I = 1 \\ \sum_{I=1}^{N_n} N_I \vec{x}_I = \vec{x} \end{cases}$$

where $H(N_I)$ is the entropy of the system of nodes following the definition given by Shannon (1948) [28], the shape function width is defined as $U(\vec{x}_p, N_I) := \sum_I N_I |\vec{x}_p - \vec{x}_I|^2$, and β is a regularisation o *thermalization* parameter such that for Pareto optimal solutions $\beta \in (0, \infty)$. Notice that β has units of $[L]^{-2}$, and can be controlled by adjusting a dimensionless parameter[3], $\widehat{\gamma} = \beta h^2$, where h is defined as a suitable measure of the nodal spacing. With the restrictions of the Pareto set, the unique solution of the local *max-ent* problem LME$_\beta$ is,

$$N_I^*(\vec{x}) = \frac{\exp\left[-\beta\,|\vec{x} - \vec{x}_I|^2 + \vec{\lambda}^* \cdot (\vec{x} - \vec{x}_I)\right]}{Z(\vec{x}, \vec{\lambda}^*)}, \tag{7}$$

where $Z(\vec{x}, \vec{\lambda}^*)$ is the *partition function* defined as,

$$Z(\vec{x}, \vec{\lambda}) = \sum_{I=1}^{N_n} \exp\left[-\beta\,|\vec{x} - \vec{x}_I|^2 + \vec{\lambda} \cdot (\vec{x} - \vec{x}_I)\right], \tag{8}$$

and a Lagrange multiplier $\vec{\lambda}^*$ such minimise the function $\log Z(\vec{x}, \vec{\lambda})$. The traditional way to compute the optimal value of $\vec{\lambda}^*$ is through a Newton-Raphson procedure, or in more challenging scenarios by a combination of the Newton-Raphson and the Nelder-Mead Simplex algorithms [22]. Nonetheless, since finite strains are not involved in the present research, Newton-Raphson is an enough efficient method. For an uniform nodal spacing, β can be considered constant, thus first derivatives of the interpolation technique ∇N_I^* can be obtained by evaluating the following expression

$$\nabla N_I^* \quad = \quad -N_I^* \left(\mathbf{J}^*\right)^{-1} (\vec{x} - \vec{x}_I) \tag{9}$$

---

[3] To avoid confusion with the γ parameter of the NPC, the dimensionless parameter defined in Arroyo & Ortiz [25] as γ will be represent by $\widehat{\gamma}$ to preserve as much as possible the original notation.

where $\mathbf{J}$ is the Hessian matrix, defined by

$$\mathbf{J}(\vec{x},\vec{\lambda},\beta) \equiv \frac{\partial \vec{r}}{\partial \vec{\lambda}}, \tag{10}$$

$$\vec{r}(\vec{x},\vec{\lambda},\beta) \equiv \frac{\partial \log Z(\vec{x},\vec{\lambda})}{\partial \vec{\lambda}} = \sum_{I}^{N_n} p_I(\vec{x},\vec{\lambda},\beta)\,(\vec{x}-\vec{x}_I). \tag{11}$$

An additional remark concerning the support of the interpolation function is that, in practice, the value of N_I decay exponentially following $\exp(-\beta\vec{r})$. In this sense, a good practice is to truncate it under a tolerance (typically around 10^{-6}) that would ensure a reasonable range of neighbours, see [25] for details. This tolerance defines a limit value of the influence radius to find the neighbour nodes of a given integration point.

2.3. Fracture modelling approach

Within the MPM formulation context, fracture can be modelled by failing particles according to a suitable failure criterion. When material points are failed, they are assumed to have null stress tensor. To reproduce this behaviour in the present research, the eigensoftening algorithm is introduced in the MPM framework as an alternative approach to the decohesion model [5]. The eigensoftening concept was developed initially by Navas *et al.* (2017)[21] as an extension for quasi-brittle materials of the eigenerosion proposed by Pandolfi & Ortiz (2012)[19] for fracture of brittle materials. The evaluation of both approaches [21] against experimental measures show that the eigenerosion algorithm significantly overestimates the tensile stress and the strain peaks, Meanwhile eigensoftening captures the forces and crack patterns accurately. Furthermore, the accuracy of this algorithm has been proven for mixed-mode fracture patterns such as the ones obtained with Fiber Reinforced Concrete (FRC), [29].

The key idea behind the eigenerosion algorithm is the computation of the energy-release rate attendant to the failure of material point p,

$$G_p^{k+1} = \frac{C_\epsilon}{m_p^{k+1}} \sum_{x_q^{k+1}\in B_\epsilon(x_p^{k+1})} m_q W_q^{k+1} \tag{12}$$

$$m_p^{k+1} = \sum_{x_q^{k+1}\in B_\epsilon(x_p^{k+1})} m_q \tag{13}$$

where $B_\epsilon(x_p^{k+1})$ is a ^{n}dimensional sphere of radius ϵ centered at x_p^{k+1}. The particles which lie under this sphere are known as the ϵ-neighborhood of the

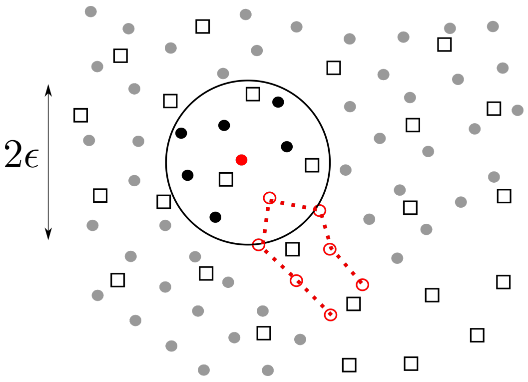

Figure 1: Scheme of a linear cohesive law, where the shaded area is G_F, f_t is the tensile strength, and w_c is the critical opening displacement.

material point (see [19]). This concept is conveniently sketched in Figure 1. Other parameters are the mass of the neighborhood m_p^{k+1}, the current free-energy density per unit mass W_q^{k+1} and the normalizing constant C_ϵ, which also defines the ϵ-neighborhood size, being $\epsilon = C_\epsilon h$, and h is a measure of the distance between nodes.

The failure criterion considers that a material point fails when G_p^{k+1} surpasses the critical energy release rate that measures the material-specific energy, G_F. The convergence of this approach has been analyzed by Schmidt *et al.* (2009)[18], who proved that G_F converges to the Griffith fracture when the discretisation size tends to zero. It is necessary to point out that, when a material point overpass the critical energy, its contribution to the internal forces vector is set to zero. However, its contribution to the mass matrix is preserved.

As can be noticed, the eigenerosion algorithm relies over an energetic failure criterion. Because of this, unrealistic stress concentration (higher than tensile strength) appears in quasi-brittle materials [21]. To overcome this limitation, the authors [21] proposed the eigensoftening approach to consider the gradual failure in quasi-brittle materials. The cohesive fracture inspires the idea behind this concept. This gradual failure criterion is plotted in Figure 2, where a linear decreasing cohesive law is presented to illustrate the concept earlier described. In the picture, the shaded region represents the static fracture energy per unit of area, G_F. Notice how a cohesive crack appears when the maximum tensile strength, f_t, is reached. Once the crack, w_n, reaches the value of the critical crack opening, w_c, a stress-free crack is attained. For the eigensoftening algorithm, a strength criterion for crack initialization was adopted. Particularly the maximum principal stress theory

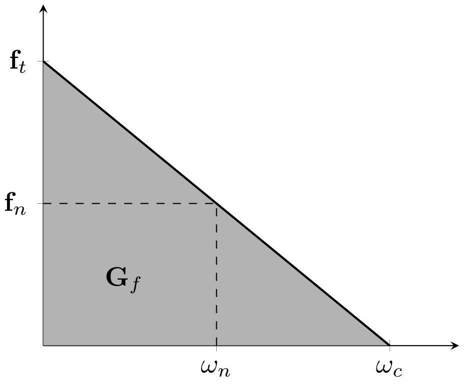

Figure 2: Scheme of a cohesive linear law, where the shaded area is G_F, f_t is the tensile strength, and w_c is the critical opening displacement.

for brittle fracture was considered in [21], this allows to quantify the variation of the averaged strain energy density in the ϵ-neighborhood of the material point $\vec{x}_p^{k+1}$ as

$$\delta W_{\epsilon,p} = \frac{\partial G_p}{C_\epsilon} = \frac{1}{m_p} \sum_{x_q^{k+1} \in B_\epsilon(x_p^{k+1})} m_q \sigma_{q,I} \delta\varepsilon_q, \tag{14}$$

where $\sigma_{q,I}$ is the maximum principal stress of each material point in the ϵ-neighborhood. At this point, an *effective* strain $\delta\epsilon$ is introduced in order to obtain the variation of the local strain energy as $\delta W_q = \sigma_{q,1}\delta\epsilon_q$. Now, with the assumption that the effective strain of each material point at every time step is constant in the neighbourhood of $\vec{x}_p^{k+1}$, the equation (14) can be simplified to

$$\delta W_{\epsilon,p} = \frac{\delta\epsilon_p}{m_p} \sum_{x_q^{k+1} \in B_\epsilon(x_p^{k+1})} m_q \sigma_{q,I}. \tag{15}$$

Consequently, it is possible to define an equivalent critical stress at the material point $\vec{x}_p^{k+1}$ as

$$\sigma_{\epsilon,p} = \frac{1}{m_p} \sum_{x_q^{k+1} \in B_\epsilon(x_p^{k+1})} m_q \sigma_{q,I}, \tag{16}$$

where m_p is the total mass of the ϵ-neighborhood, defined similarly to the eigenerosion method (Eq. (13)). The equivalent critical stress leads to a definition of the averaged strain energy in terms of the averaged strain as

$\delta W_{\epsilon,p} = \sigma_{\epsilon,p}\ \delta\epsilon_p$. The softening behaviour is activated once $\sigma_{\epsilon,p}^{k+1}$ surpasses the tensile strength, f_t. This consists of a reduction of the internal forces as,

$$f_I^{int} = \sum_p (1 - \chi_p)\ \sigma_p^{k+1} \cdot grad(N_{Ip})\ \Omega_p, \tag{17}$$

where χ_p and Ω_p are respectively the damage or softening variable and the volume for each material point p. χ_p is any function, taking values between zero (an intact material) and one (completely failed material points), that relates the crack opening and the residual strength. Typical shapes of cohesive laws such as linear, bilinear or exponential may be employed to calculate it. For the case of a linear softening such the sketched one in the Figure 2, χ_p is computed as,

$$1 - \chi = \frac{f_n}{f_t} = 1 - \frac{w_n}{w_c} \ \rightarrow\ \chi = \frac{w_n}{w_c}. \tag{18}$$

Analogous to the crack band model presented by Bazant [23], Navas *et al.* [29] [21] introduced a band width parameter h_ϵ in order to relate the crack opening with the strain. Concerning this parameter, a typical value between two and four times the maximum size of the aggregates is adopted in the case of concrete as brittle material. The effective fracture strain $\varepsilon_{\epsilon,f}$ is defined as the difference between the strain at crack initialization, $\varepsilon_1(\vec{x}_p^0)$, and the current strain, $\varepsilon_1(\vec{x}_p^{k+1})$, for a material point p. Also, $\varepsilon_{\epsilon,f}$ can be represented as the current crack opening w_n within the band width h_ϵ. Therefore,

$$\varepsilon_{\epsilon,f} = \varepsilon_1(\vec{x}_p^{k+1}) - \varepsilon_1(\vec{x}_p^0) = \frac{w_n}{h_\epsilon} \tag{19}$$

Introducing (19) in (18), the damage variable can be computed as,

$$\chi = \frac{\varepsilon_{\epsilon,f}\ h_\epsilon}{w_c}. \tag{20}$$

The function of χ presented in (20) represents a linear softening behaviour. For a general case, the damage variable can be expressed in terms of the following variables,

$$\chi = \chi(\varepsilon_{\epsilon,f}, h_\epsilon, f_t, w_c, G_f) \tag{21}$$

Implementation details can be consulted in Appendix B. Unfortunately, this method is not free of pitfalls. The first one involves the isotropic model of failure assumption of the eigensofteing, therefore, complex fracture patterns such as delamination can not be simulated. A possible solution for this inconvenience is the use of anisotropic damage model. Regarding this, the current work can be extended following the approach proposed by Nairn [7]. The second one is handling crack contact. After the particle fails, the stress tensor of it is enforced to be zero in all the directions. Of course, this is a direct consequence of the isotropic model of failure assumption. Consequently, a spurious slip condition is enforced in the tangent direction of the crack, also the material loose its toughness to compression in the fracture interface. This limitation was noticed earlier by in Pandolfy and Ortiz [19] where alternatives to overcome this limitation were briefly discussed. Again, the use of an anisotropic damage model [7] would overcome this limitation.

2.4. ϵ-neighbourhood reconstruction : A node-linked method

The construction of the ϵ-neighbourhood is a major issue of the proposed methodology. Since this operation could be extremely demanding, optimal numerical implementation should be employed. In opposite with the Cell-linked method proposed by Allen & Tildesley [30] where the definition of a numerical tolerance is required for auxiliar algorithms, the proposed methodology adopted herein is linked to the shape function neighbourhood. In order to avoid error prone techniques such those mentioned before, we endeavour to exploit the meshfree benefits of the LME approximants to introduce a node-linked method.

The standard version of the MPM has a well defined nodal connectivity since the elements in the background mesh are defined locally. So far, most implementations of the MPM relies on this. Nevertheless, due to the global support of the LME approximants, the rigid concept of element connectivity vanish in favour of a more flexible and mesh-free interpretation of the connectivity. First, let us define the concept of a particle *tributary nodes* as the list of nodes close to it among which the information transfers occur. To improve computational efficiency, a linked list with the surrounding nodes for each node is defined at the initial time. Also, each particle is related with the closest node instead of belonging to an element. This is radical change in the way of search algorithm has been implemented heretofore. Once the closest nodes are defined, the particle possesses automatically a list of *tributary nodes*. This has two immediate benefits: the first one is that shape functions with global support as LME are easier to be implemented, and the second one is the increase of the efficiency of the ϵ-neighbourhood reconstruction. Regarding this last benefit, since the current particle has a *tributary nodes* list assigned to it, and consequently each node has a linked list with a set of *tributary particles*[4] close to it, it is possible to define effi-

---

[4] Notice that the list of the particles close to each node is unique for each node and is

ciently a search list with those particles close to the current particle. In the end, particles out of the area of influence, Figure 1, are pop out of the final ϵ-neighbourhood. A final remark about this new approach is its ability to reconstruct easily a search list with the support of the initial connectivity of the mesh. It provides a suitable basis for an easy implementation of other interpolation techniques with minimum coding effort. A detailed explanation of the proposed algorithm can be found in Appendix C.

3. Cases of study and discussion

The proposed approach to overcome the two main shortcomings of Eighen-MPM has been evaluated with three benchmark tests. On the one hand, the benchmark proposed in section 3.1 discusses the presence of stress instabilities provoked by the spatial discretisation. For that purpose, two different interpolation techniques, GIMP and LME, has been compared by carrying out an eigenerosion simulation. On the other hand the inability of the eigenerosion to simulate quasi-brittle fracture properly is discussed in sections 3.2 and 3.3, where experimental results are compared with numerical ones. The case proposed in section 3.2 is a semicircular bending test, and in section 3.3, a drop-weight impact test.

3.1. Edge-cracked square panel in mode I

The aim of the problem presented in this section is to assess the capability of the LME approximants to improve the result *versus* the standard linear interpolation and uGIMP [31]. The application consists of a square plate of size $H = 1$ containing an initial edge crack of length $0.25 \cdot H$ loaded in a pure mode I by displacement control on the outer flanks of the plate (See Figure 3 for details). The constitutive model considered in the numerical experiment is a linear-elastic Hookean material, whose Young's modulus E $= 1.06$, the Poisson's ratio $\nu = 0.333$, and critical energy-release rate $\mathrm{G}_F = 0.0001$. The absence of units is due to the current simulation will not be tested against experimental results, where scale factor is relevant, but will be validated against an analytical solution provided by Pandolfi & Ortiz [19]. In MPM, two different discretisation are required. On one hand, a cartesian grid of nodes is considered with a nodal spacing value of 0.025. On the other hand, the plate will be modeled with a initial layout of four particles per element and occupying the Gauss quadrature positions.

---

updated in each time step.

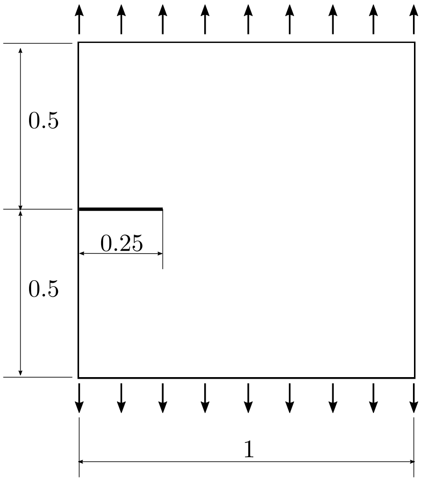

Figure 3: Geometry and boundary condition of the drop-weight impact test.

Figure 4 clearly shows that the LME$_{\gamma=3.5}$ solution has a reaction peak value of 0.03 for a imposed displacement 0.015 which agrees with the analytical solution [19]. It also shows the presence of wiggles in the reaction-displacements curve, in both loading and post-failure stages, when linear interpolation technique is used. In contrast, LME simulation does not exhibit these spurious oscillations and remains linear until the failure. About the strength, linear interpolation produces stiffer results than LME. This over stiffening can be attributed to imprecision in the stress field due to grid-crossing phenomena. Alternative to LME, uGIMP shape functions can be employed to mitigate grid-crossing instabilities. Figure 4 supports this fact since it does not exhibit instabilities when particles cross element borders meanwhile these instabilities are found with linear interpolation. Unfortunately, the extended support of this kind of shape function interfere with nodes in both sides of the notch, producing an undesired “tie-effect”. This involves in a violation of the free border boundary condition in the notch. Possible solutions to this effect are the suppression of the elements in the notch, within a CRAMP-like method where two pairs of nodes are employed, or reducing the mesh size. With LME approximants these artifices are not required since it is possible to control the support of the shape function reducing the grid-crossing and to avoid the“tie-effect” at the same time.

Additionally, Figure 5 remark clearly the difference between linear interpolation and LME, since numerical instability becomes rather significant when particles crosses the boundary of the element in the linear case, which is observed at 60 seconds. Although, the differences in the obtained peaks are not extremely significant, it can be owing to the aforementioned hookean

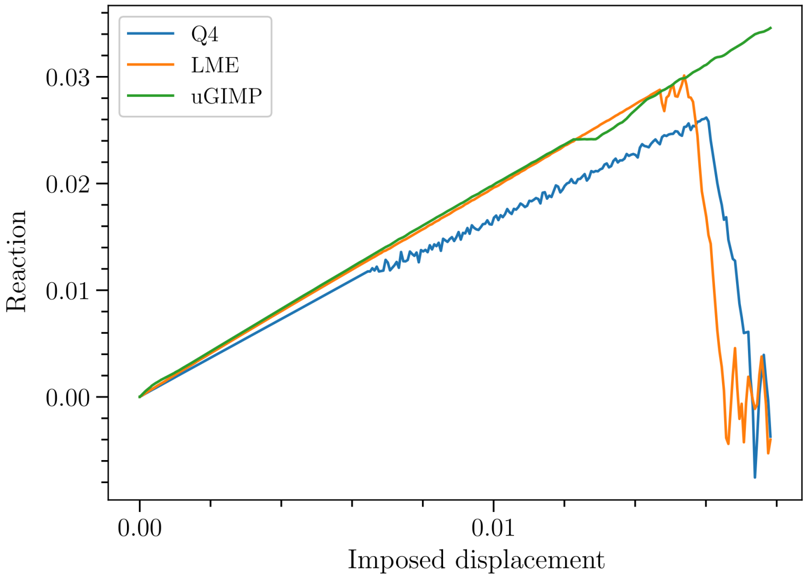

Figure 4: Evolution of the reaction forces plotted *versus* the imposed displacement for linear interpolation technique and the LME approximants.

material employed [20]. When more sophisticated constitutive models will be employed, severe inaccuracies may appear in the stress field that could affect dramatically to the final result. Focusing on the post failure behavior, it can be seen how LME produces soft stress field evolution even after breaking. An important consideration regarding the presence of oscillations once both parts of the panel are separated is observed in Figure 4. These phenomena should not be attributed to the eigenerosion algorithm since the fracture process is over. These oscillations are due to the dynamic nature of the solver: once the energy is released dinamically by the crack, the waves propagate along the domain.

3.2. Semicircular bending test

The second application to be considered analyses the bending behavior of semicircular specimens of Johnstone rocks, text which were experimentally carried out by Lim *et al.* [32] and numerically reproduced by Wang *et al.*[10] under SPH framework within an implicit algorithm. The test aims to examine the predictive capability of the eigensoftening algorithm under different kind of mixed-mode loading conditions.

The geometry and boundary conditions are sketched in Figure 6. The experiment consist of loading semicircular specimens with a radius of 47.5 mm and a thickness of 20 mm, and supported by two rollers at a span of

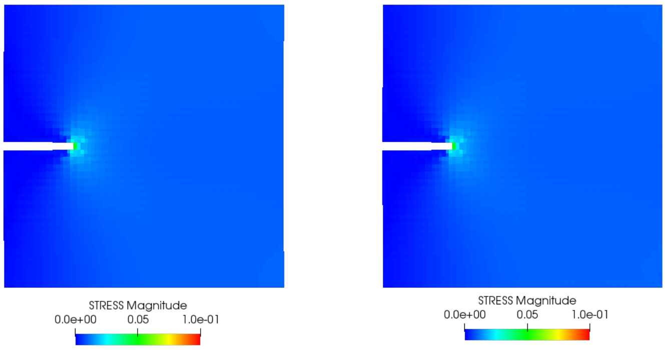

(a) t = 25

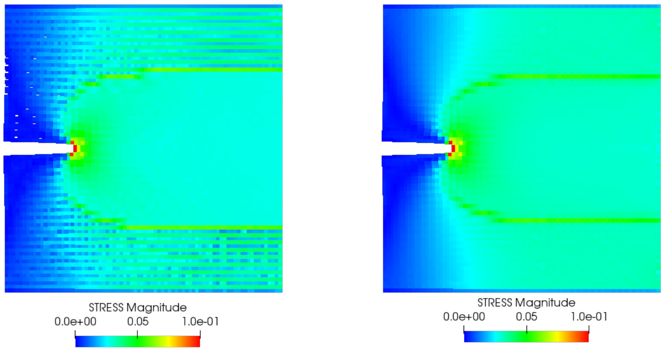

(b) t = 60

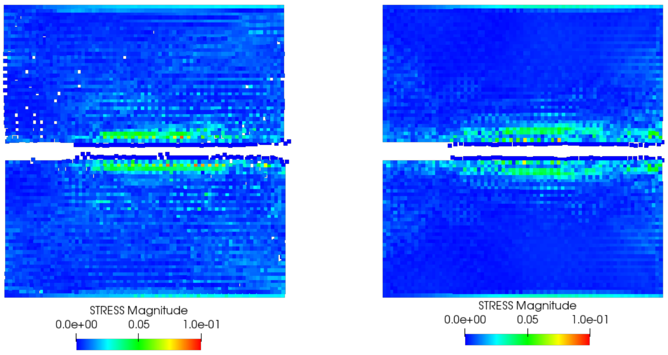

(c) t = 100

Figure 5: Evolution of the stress tensor magnitude for linear interpolation (pictures in the left side), and LME (pictures in the right side). The results are printed directly on the material points.

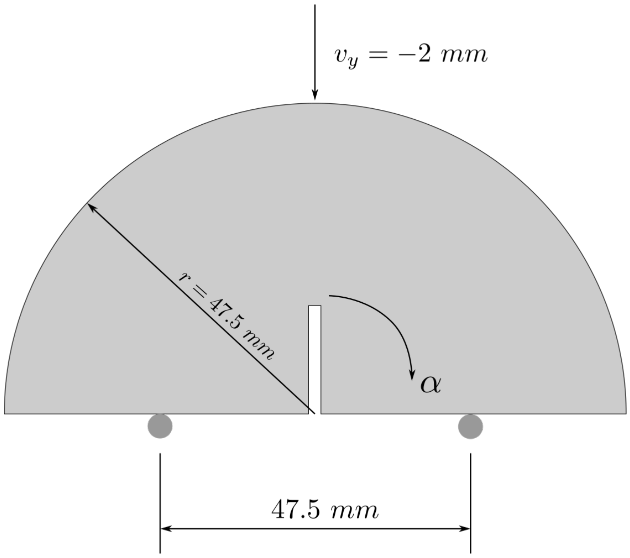

Figure 6: Geometry and boundary condition of the semicircular bending test.

Young's modulus (E)	0.4 GPa
Poisson ratio (ν)	0.25
Density (ρ)	1.54 $\mathrm{g/cm^3}$
Tensile strength (f_t)	0.6 MPa
Critical opening displacement (w_c)	0.015 mm

Table 1: Material properties of Johnstone.

47.5 mm, by another roller on its top mid-span. Notches with a length of 16.6 mm are created with the different notch angles of 0°, 30° and 60° with respect to the vertical axis in order to investigate the influence of the notch angle on the peak load 8. The material properties of Johnstone rock are listed in Table 1. In the tests, particles were uniformly distributed with an almost constant separation of 1 mm between them, resulting in a total number of 4672 MPM particles for generating the specimen. Additionally, a regular cartesian background grid of 1917 nodes with 1.5 mm of nodal distance was generated. The velocity of the particles in the top boundary is $v_y = 2mm/s$, whereas the velocity of the bottom boundary particles is $v_y = 0mm/s$. This boundary condition has been imposed via a soft loading ramp to ovoid dynamic effects due to a sudden loading. Finally, the model was calibrated with a regularization parameter $\mathrm{C}_\epsilon = 1.7$ and a bandwidth value $\mathrm{h}_\epsilon = 15$.

Figure 7 compares the comparison of mixed-mode fracture envelope between experiments and MPM simulations for different notch inclination an-

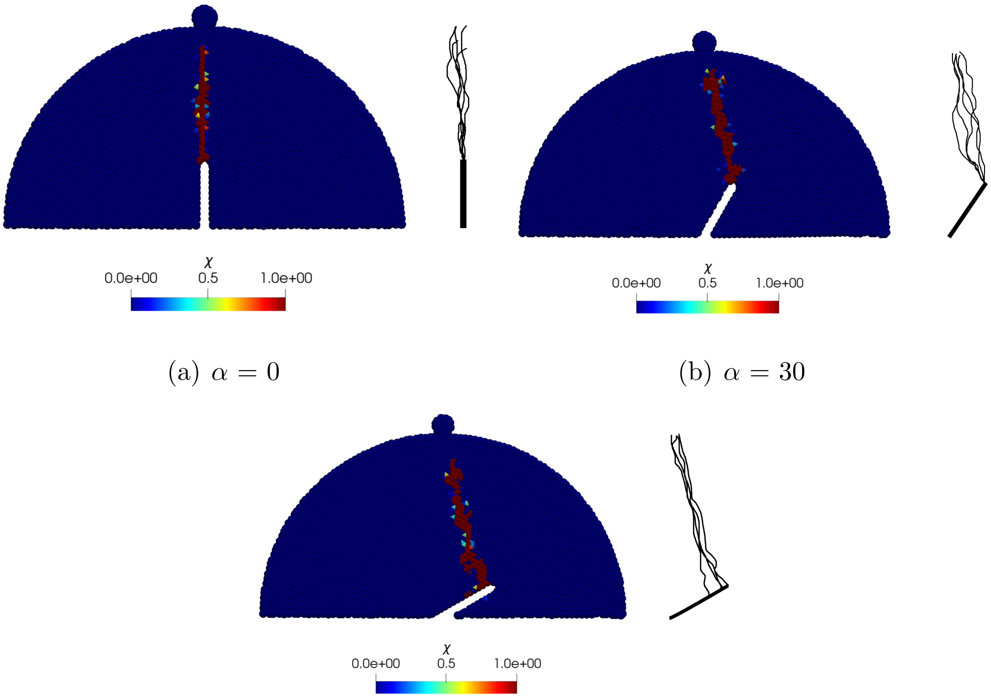

(a) $\alpha = 0$

(b) $\alpha = 30$

(c) $\alpha = 60$

Figure 7: Crack pattern for different notch inclination angle, and comparison with the experimental results [32]. The results are printed directly on the material points.

gles $\alpha = 0°$, $30°$ and $60°$. The final fracture pattern is a vertical straight line when $\alpha = 0°$ (pure mode I). When $\alpha > 0°$, the sample is subjected to a mixed-mode pattern. For the cases of $0°$ and $30°$, cracks initiate from the notch tip and then propagate towards upper loading point. Experiments show that a few cracks tend to initiate behind notch tip when the notch angle is beyond $50°$. Figure 7 demonstrates that eigensoftening, combined with MPM, can to reproduce this behavior. Therefore, the simulation results predict successfully the fracture envelope in experiments and highlight the capability of the eigensoftening-MPM for capturing the fracture development under various complex loading conditions. Additionally, 8 compare the peak load between experiments and simulations for the notch inclination angles $0°$, $30°$ and $60°$. This figure proofs how the eigensoftening-MPM simulation can appropriately capture the increasing trend of the peak load with the increasing notch angles in the experiment.

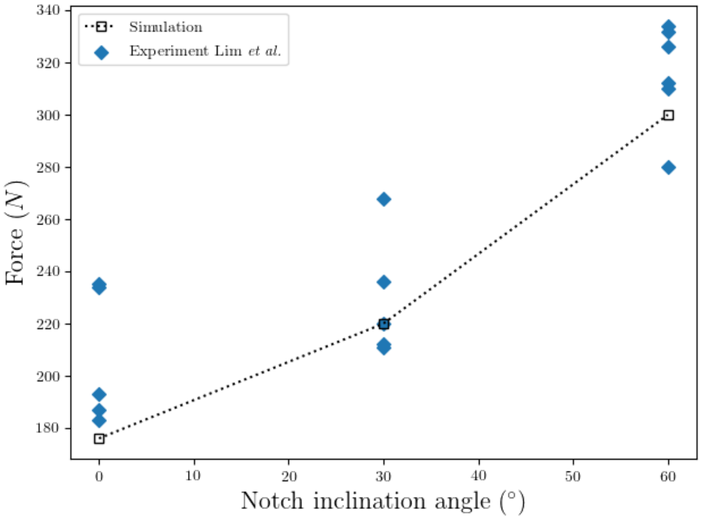

Figure 8: Numerical results compared with the experimental results [32].

3.3. Drop-weight impact test

This section is devoted to proof the accuracy of the eigensoftening algorithm within the MPM framework when the behavior of quasi-brittle materials under dynamic loading is simulated. One of the most interesting examples of this loading case is the three-point bending test on a concrete notched beam when conducted under impact loading. Indeed, this experimental test is appropriate to be reproduced numerically with the explicit solver proposed in this paper since fracture occurs in a period of milliseconds and waves propagate fast along the high strength materials involved in the test. Accordingly, small time steps are required to achieve a numerically stable simulation.

An interesting case of this experimental test was reported by Zhang *et al.* [33]. As in this study, an impact hammer of 120.6 kg has been employed in the proposed simulations to drop it at an impact speed of 2640 mm/s. The beam dimensions were 100 mm x 100 mm (B x D) in cross section, and 420 mm in total lenght (L). The initial notch-depth ratio was approximately 0.5, and the span, S, was fixed at 300 mm during the tests (see Figure 9). The material adopted for the simulation was characterised by Navas *et al.* [21], being the material properties, such as the material density, ρ, the compressive strenght, f$_c$, the tensile strenght f$_t$, the specific fracture energy, G$_F$, and the elastic modulus E, provided in table 2.

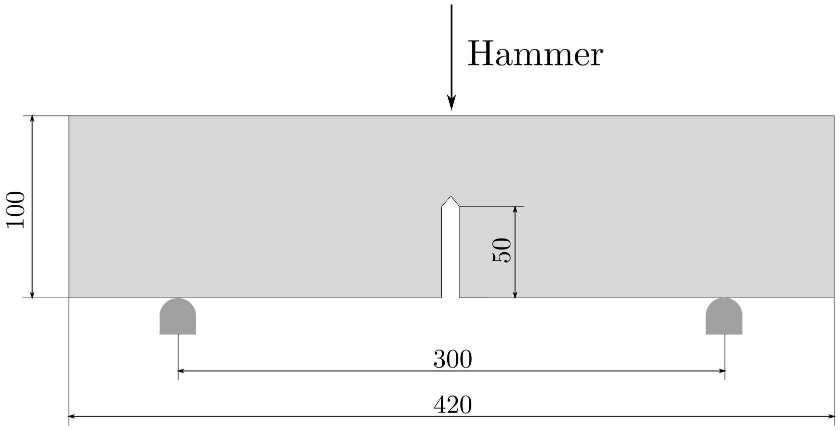

Figure 9: Geometry and boundary condition of the drop-weight impact test.

	ρ (kg/m^3)	f$_c$ (MPa)	f$_t$ (MPa)	G$_F$ (N/m)	E (GPa)	d$_{max}$ (mm)
Value	2368	102.7	5.4	141	31	12

Table 2: Mechanical properties of the high strenght concrete.

For the present research, a 2D setting of the experiment has been adopted. Both the hammer and the concrete beam are explicitly represented in order to properly capture the impact. Several levels of discretisation were required to assess the objectiveness of the obtained results. The results here exposed are from a discretisation of 21576 material points and 3943 nodes. To achieve better results, an unstructured grid layout has been adopted focusing the minimum nodal spacing, 1.2 mm, in the middle of the beam and in the impact surface of the hammer. For this simulation, $\widehat{\gamma}$ was fixed to 1.8, this low value of the regularization parameter smooth high stress overshots after the impact. Here the stabilization properties of the LME described in [24] becomes crucial to achieve non-spurious results. Standard linear element were tested with unsatisfactory results since grid-crossing occurs in the hammer head producing non realistic forces.

First, the reaction and impact forces are validated against their experimental counterparts. Since the impact forces applied by the hammer and the reaction forces at the two supports were experimentally measured, they are compared with numerical ones in Figure 10. Note that the general trend of the impact forces was correctly captured. Although the traditional MPM implementation allows collision of two bodies, inaccurate energy conservation is obtained without implementing of a conservative contact algorithm

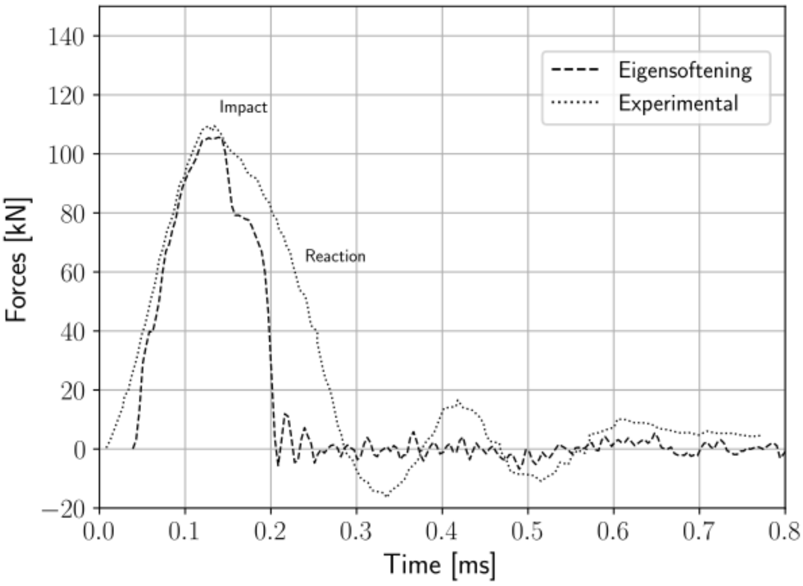

(a) Hammer forces

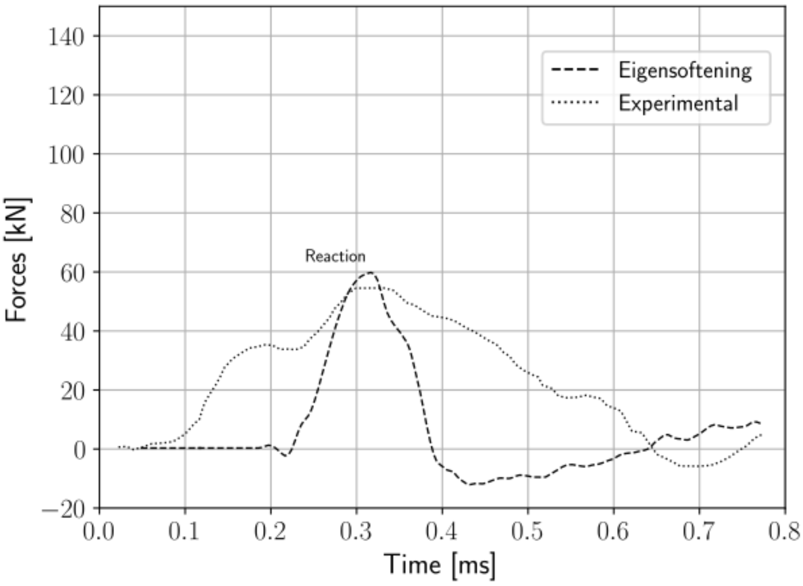

(b) Reactions

Figure 10: Comparison of eigensoftening *versus* experimental results.

to reproduce the hammer impact in the beam. Despite the observed discrepancies, this is out of the scope of this paper, although future research of authors will overcome this limitation. Similarly, results of support forces will be more realistic when modelled by a suitable contact algorithm instead of avoiding any vertical displacement. Navas *et al.* (2017)[21] demonstrate the importance of the stiffness of the support in order to obtain accurate results of the reaction forces. Interesting contact algorithms within the MPM methodology are available in the literature [34, 35].

Finally, longitudinal stress distribution and crack propagation are depicted in Figure 11. Stress evolution agrees with the results obtained by [21] under the OTM framework. Two additional considerations about this results are concerning the interpolation technique.

On the one hand, in the opposite to the uGIMP shape function, LME allows unstructured grids without a considerable computational cost or any additional accommodation in the formulation. This is suitable for those simulations where the majority of the computation efforts are located in a small region of the domain. On the other hand, there is the possibility of reducing the shape function support to avoid the ”tie-effect” due to a non-convex domain.

4. Conclusions

The paper proposes the eigensoftening algorithm in a MPM framework for quasi-brittle materials to overcome the EigenMPM [20] limitations. The overestimation of tensile stress and strain peaks in the fracture mechanism of quasi-brittle materials and the stress oscillations observed with conventional MPM are faced. Based on the EigenMPM approach to fracture, two additional improvements have been proposed in the present research to solve the shortcomings of the original concept pointed out in [20].

Firstly, by introducing the concept of eigensoftening to the MPM framework allows capture the failure process of each material point. This concept is analogous the softening law which is traditionally employed in the context of cohesive fracture in FEM. Furthermore, this failure criterion admits the design of more elaborated damage curves, which can be employed in order to describe the failure process in more sophisticated materials. Secondly to achieve better results, three new numerical algorithms has been implemented. The LME approximants are employed to remove from the solution those wiggles provoked by inaccuracies in the stress integration and to avoid the “tie-effect” observed in the uGIMP. The traditional time scheme of the MPM has been improved with a Newmark Predictor Corrector scheme as well. And the traditional concept of element connectivity has been removed

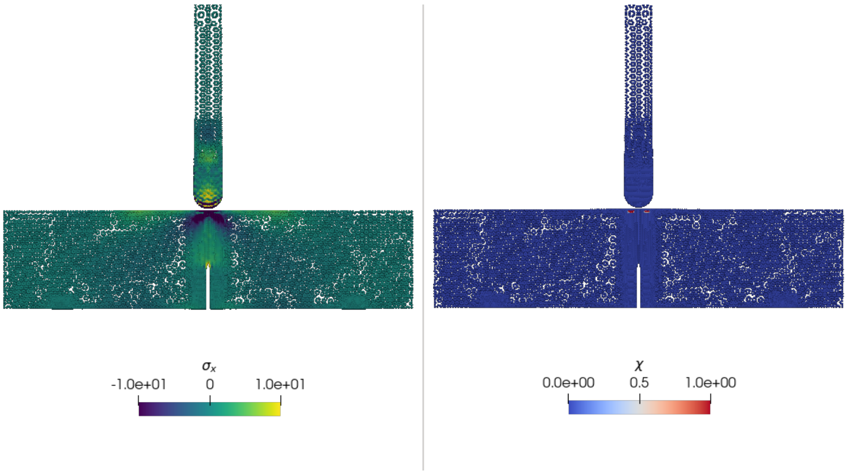

(a) t = 0.27 ms

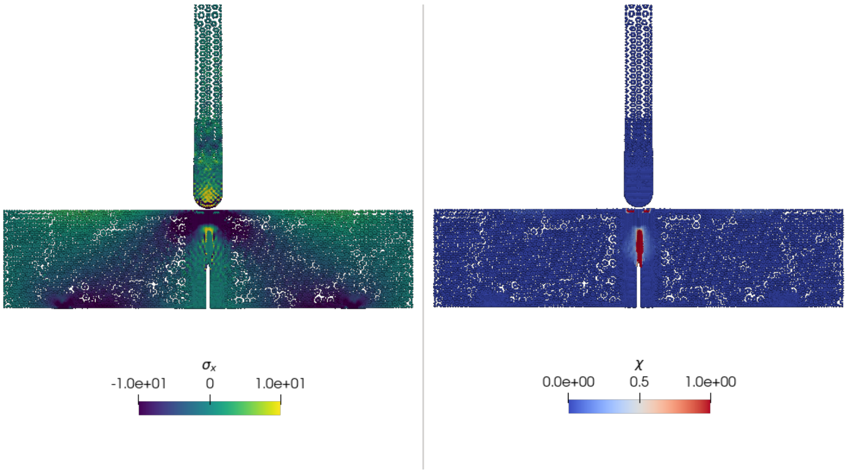

(b) t = 0.36 ms

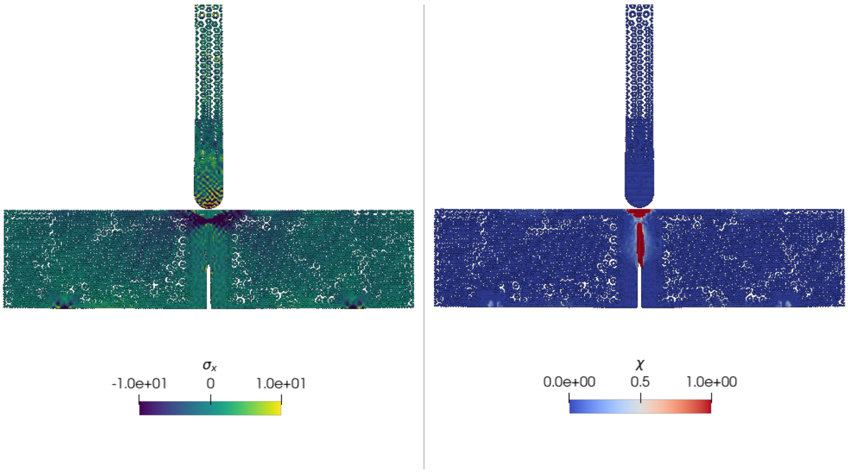

(c) t = 0.45 ms

Figure 11: Evolution of the stress tensor magnitude [MPa] for linear interpolation (pictures in the left side), and LME (pictures in the right side). The results are printed directly on the material points.

to allow a more flexible and efficient implementation of search algorithm. In this research, the aforementioned techniques have helped to improve the results in fracture propagation through the eigensoftening and eigenerosion algorithms.

Next, further improvements of the present research are exposed. First, the eigensoftening approach can be extrapolated to rock fracture in the same manner the eigenerosion was [36], taking into account that the volumetric stiffness remains in order to support bulk loads. Secondly, the algorithm would have the ability to simulate of crack patterns in composite material such as steel or carbon fiber reinforced concretes by means of empirical definitions of χ curve [29]. However, capturing fracture patterns in anisotropic media such as carbon fibre plates requires the redefinition of the approximation towards an anisotropic softening damage model. In addition, this improvement would also allow the model to handle crack contact. Finally, the implementation of a contact algorithm to model other impact cases such as bullets collisions would improve the accuracy of such problems.

Acknowledgements

The financial support to develop this research from the Ministerio de Ciencia e Innovación, under Grant No. BIA-2016-76253 is greatly appreciated. The first and the second authors also acknowledge the fellowship Fundación Agustín de Betancourt and Juan de la Cierva (FJCI-2017–31544) respectively.

Glossary

β Regularization or thermalization parameter of the LME$_\beta$ Pareto set. 6, 24

$\delta\epsilon$ Effective strain. 9

ϵ Neighbourhood size. 7–9

γ Time integration parameter for the NPC algorithm. 4, 6

ν Poisson ratio. 12, 16

ρ Describes the scalar density field. 16, 18

σ Second order tensor which means the Cauchy stress tensor. 3

ε Second order tensor which means the Cauchy strain tensor. 3

$\varOmega$ Continuum domain. 3

$\mathbf{v}$ First order tensor which describes the velocity field. 3

$\mathbf{x}$ First order tensor which describes the global coordinates field. 3

$\widehat{\gamma}$ Dimensionless parameter to control the value of the thermalization parameter β of the LME shape functions.. 6, 19

m Describes the scalar mass field. 3

w_c Critical opening displacement. 8, 9, 16, 27

w_n Current crack opening. 8, 10

$\mathbf{C}_\epsilon$ Normalizing constant. 8, 16

$\mathbf{E}$ Elastic modulus. 12, 16, 18

$\mathbf{f}_c$ Compressive strenght. 18

$\mathbf{f}_t$ Tensile strenght. 8–10, 16, 18

$\mathbf{G}_F$ Specific fracture energy. 8, 9, 12, 18, 19

$\mathbf{h}_\epsilon$ Band width. 10, 16

Acronyms

CRAMP CRAcks with Material Points. 2

EFGM Element-Free Galerkin Method. 2

FEM Finite Element Method. 1, 4, 21

FRC Fiber Reinforced Concrete. 7

GIMP Generalized Interpolation Material Point. 3, 12

LME Local Maximum-Entropy. 3, 5, 6, 11–15, 19, 21, 22, 24

MPM Material Point Method. 1–4, 7, 11, 12, 16–19, 21

NPC Newmark Predictor-Corrector. 3, 6, 23

OTM Optimal Transportation Meshfree. 1–3, 21

SPH Smoothed Particle Hydrodynamics. 2, 14

uGIMP Uniform GIMP. 12, 13, 21

XFEM Extended Finite Element Method. 1, 2

Appendix A. Explicit Newmark Predictor-Corrector algorithm

```
Update mass matrix : $\mathbf{m}_I = N_{Ip}^k \; m_p$
Explicit Newmark Predictor :
    $\vec{v}_I^{pred} = \sum_{p \, \in \, \mathcal{C}} \frac{N_I(\vec{x}_p^k) \; m_p \; (\vec{v}_p^k + (1-\gamma) \; \Delta t \; \vec{a}_p^k)}{m_I}$
Impose essential boundary conditions : At the fixed boundary, set $\vec{v}_I^{pred} = 0$.
Deformation tensor increment calculation :
    $\Delta\varepsilon_p^{k+1} = \Delta t \; \dot{\varepsilon_p}^{k+1} = \sum_{I \, \in \, \mathcal{B}_p} \Delta t \; \left[\vec{v}_I^{pred} \otimes grad(N_I(\vec{x}_p^k))\right]^s$
Update the density field : $\rho_p^{k+1} = \frac{\rho_p^k}{1+tra\left[\Delta\varepsilon_p^{k+1}\right]}$.
Compute stress field and update damage parameter
Balance of forces calculation : Calculate the total grid nodal force $\vec{f}_I^{k+1} = \vec{f}_I^{int,k+1} + \vec{f}_I^{ext,k+1}$.
Explicit Newmark Corrector :
    $\vec{v}_I^{k+1} = \vec{v}_I^{pred} + \gamma \; \Delta t \; \frac{\vec{f}_I^{k+1}}{\mathbf{m}_I^{k+1}}$
Update particles lagrangian quantities :
    $\vec{a}_p^{k+1} = \sum_{I \, \in \, \mathcal{B}_p} \frac{N_I(\vec{x}_p^k) \; \vec{f}_I^k}{\mathbf{m}_I^k}$
    $\vec{v}_p^{k+1} = \vec{v}_p^n + \sum_{I \, \in \, \mathcal{B}_p} \Delta t \; \frac{N_I(\vec{x}_p^k) \; \vec{f}_I^k}{\mathbf{m}_I^k}$
    $\vec{x}_p^{k+1} = \vec{x}_p^n + \sum_{I \, \in \, \mathcal{B}_p} \Delta t \; N_I(\vec{x}_p^k) \; \vec{v}_I^k + \frac{1}{2}\Delta t^2 \; \frac{N_I(\vec{x}_p^k) \; \vec{f}_I^k}{\mathbf{m}_I^k}$
Reset nodal values
```

Algorithm 1: Explicit Newmark Predictor-Corrector scheme

Appendix B. Eigensoftening Algorithm

```
Input: For each $p$, $\epsilon$-neighbourhood, $f_{t,p}$, $h_{\epsilon,p}$, $w_c$
Output: Return damage parameter $\chi = \{\chi_p\}$
Data: Testing set $x$
$\chi_p \leftarrow \chi_p^k$
for $p$ to $N_p$ do
    if $\chi_p = 0$ and $\epsilon_{f,p} = 0$ then
        for $q \in B_{\epsilon,p}$ do
            $\sigma_{q,I} \leftarrow$ getEigenvaluesOf($\sigma_q$)
            if $\chi_q < 1$ then
                $\sum m_p \sigma_{p,I} \leftarrow \sum m_p \sigma_{p,I} + m_q \sigma_{q,I}$
            end
            $m_p \leftarrow m_p + m_q$
        end
        $\sigma_{p,\epsilon} \leftarrow \frac{1}{m_p} \sum m_p \sigma_{p,I}$
        if $\sigma_{p,\epsilon} > f_{t,p}$ then
            $\epsilon_{f,p} = \epsilon_{I,p}$
        end
        else if $\chi_p \neq 1$ and $\epsilon_{f,p} > 0$ then
            $\chi_p^{k+1} \leftarrow \min\left\{1, \max\{\chi_p^k, \frac{(\epsilon_{I,p} - \epsilon_{f,p})\ h_{\epsilon,p}}{w_c}\}\right\}$
        end
    end
end
```

Algorithm 2: Compute damage parameter χ

Appendix C. Node-linked method for ϵ-neighbourhood reconstruction

```
Input: $I_0$ : Closest node for each particle
Input: $I_{Nodes}$ : List of nodes close to each node
Input: $Particles_I$ : List of particles close to each node
Output: neighbourhood$_\epsilon$ : $\epsilon$-neighbourhood for each particle
for $p$ to $N_p$ do
    For each $p$ get $I_0$
    Eval $I_{Nodes}(I_0)$
    for $k \in I_{Nodes}(I_0)$ do
        $\text{neighbourhood}_\epsilon^{k+1} = \text{neighbourhood}_\epsilon^{k} \cup Particles_I(k)$
    end
    for $p_\epsilon \in neighbourhood_\epsilon$ do
        if $distance(p_\epsilon, p) > \epsilon$ then
            pop $p_\epsilon$ from neighborhood$_\epsilon$
        end
    end
end
```

Algorithm 3: ϵ-neighborhood reconstruction algorithm

References

[1] M. Ortiz, A. Pandolfi, Finite-deformation irreversible cohesive elements for three-dimensional crack-propagation analysis., International Journal for Numerical Methods in Engineering. 44 (1999) 1267–1282. doi:10.1002/(SICI)1097-0207(19990330)44:9¡1267::AID-NME486¿3.0.CO;2-7.

[2] T. Belytschko, H. Chen, J. Xu, G. Zi, Dynamic crack propagation based on loss of hyperbolicity and a new discontinuous enrichment., International Journal for Numerical Methods in Engineering. 58 (2003) 1873–1905. doi:10.1002/nme.941.

[3] J. Huang, An efficient morphology generation and level set representation of cementitious microstructures with arbitrarily shaped aggregates and cracks via extended finite elements, Computers & Structures 206 (2018) 122 – 144. doi:10.1016/j.compstruc.2018.05.010.

[4] T. Nagashima, M. Sawada, Development of a damage propagation analysis system based on level set xfem using the cohe-

sive zone model, Computers & Structures 174 (2016) 42 – 53. doi:10.1016/j.compstruc.2015.10.005.

[5] H. Schreyer, D. Sulsky, S. Zhou, Modeling delamination as a strong discontinuity with the material point method, Computer Methods in Applied Mechanics and Engineering 191 (2002) 2483–2507. doi:10.1016/S0045-7825(01)00409-1.

[6] J. Nairn, Material point method calculations with explicit cracks, Computer Modeling in Engineering & Sciences 4 (6) (2003) 649–664. doi:10.3970/cmes.2003.004.649.

[7] J. A. Nairn, Direct comparison of anisotropic damage mechanics to fracture mechanics of explicit cracks, Engineering Fracture Mechanics 203 (2018) 197 – 207, 8th ESIS TC4 International Conference- Fracture of Polymers, Composites and Adhesives. doi:https://doi.org/10.1016/j.engfracmech.2018.05.047.

[8] T. Belytschko, Y. Lu, L. Gu, Crack propagation by element-free galerkin methods, Engineering Fracture Mechanics 51 (2) (1995) 295 – 315. doi:https://doi.org/10.1016/0013-7944(94)00153-9.

[9] T. Belytschko, D. Organ, C. Gerlach, Element-free galerkin methods for dynamic fracture in concrete, Computer Methods in Applied Mechanics and Engineering 187 (3) (2000) 385 – 399. doi:10.1016/S0045-7825(00)80002-X.

[10] Y. Wang, H. T. Tran, G. D. Nguyen, P. G. Ranjith, H. H. Bui, Simulation of mixed-mode fracture using sph particles with an embedded fracture process zone, International Journal for Numerical and Analytical Methods in Geomechanics 44 (10) (2020) 1417–1445. doi:10.1002/nag.3069.

[11] Y. Wang, H. Bui, G. Nguyen, P. Ranjith, A new sph-based continuum framework with an embedded fracture process zone for modelling rock fracture, International Journal of Solids and Structures 159 (2019) 40–57. doi:10.1016/j.ijsolstr.2018.09.019.

[12] A. Pandolfi, B. Li, M. Ortiz, Modeling fracture by material-point erosion., International Journal of fracture 184 (2013) 3–16. doi:10.1007/s10704-012-9788-x.

[13] B. Li, A. Pandolfi, M. Ortiz, Material-point erosion simulation of dynamic fragmentation of metals., Mechanics of Materials 80 (2015) 288–297. doi:10.1016/j.mechmat.2014.03.008.

[14] Y. D. Ha, F. Bobaru, Characteristics of dynamic brittle fracture captured with peridynamics, Engineering Fracture Mechanics 78 (6) (2011) 1156 – 1168. doi:10.1016/j.engfracmech.2010.11.020.

[15] T. Rabczuk, H. Ren, A peridynamics formulation for quasi-static fracture and contact in rock, Engineering Geology 225 (2017) 42 – 48, special Issue: Characterisation of Fractures in Rock: from Theory to Practice (ROCKFRAC). doi:10.1016/j.enggeo.2017.05.001.

[16] H. Tan, J. Nairn, Hierarchical, adaptive, material point method for dynamic energy release rate calculations, Computer Methods in Applied Mechanics and Engineering 191 (2002) 2123–2137. doi:10.1016/S0045-7825(01)00377-2.

[17] Z. Chen, W. Hu, L. Shen, X. An, R. Brannon, An evaluation of the mpm for simulating dynamic failure with damage diffusion, Engineering Fracture Mechanics 69 (2002) 1873–1890. doi:10.1016/S0013-7944(02)00066-8.

[18] B. Schmidt, F. Fraternali, M. Ortiz, Eigenfracture: an eigendeformation approach to variational fracture., SIAM J. Multiscale Model. Simul. 7 (2009) 1237–1266. doi:10.1137/080712568.

[19] A. Pandolfi, M. Ortiz, An eigenerosion approach to brittle fracture., International Journal for Numerical Methods in Engineering 92 (2012) 694–714. doi:10.1002/nme.4352.

[20] K. Zhang, S.-L. Shen, A. Zhou, Dynamic brittle fracture with eigenerosion enhanced material point method, International Journal for Numerical Methods in Engineering (2020) 1–27doi:10.1002/nme.6381.

[21] P. Navas, R. Yu, B. Li, G. Ruiz, Modeling the dynamic fracture in concrete: an eigensoftening meshfree approach, International Journal of Impact Engineering 113. doi:10.1016/j.ijimpeng.2017.11.004.

[22] P. Navas, S. López-Querol, R. C. Yu, M. Pastor, Optimal transportation meshfree method in geotechnical engineering problems under large deformation regime, International Journal for Numerical Methods in Engineering 115 (10) (2018) 1217–1240. doi:10.1002/nme.5841.

[23] Z. Bažant, B. Oh, Crack band theory for fracture in concrete., Materials and Structures. 16 (1983) 155–177. doi:10.1007/BF02486267.

[24] M. Molinos, P. Navas, M. Pastor, M. Martín Stickle, On the dynamic assessment of the Local-Maximum Entropy Material Point Method through an Explicit Predictor-Corrector Scheme, Computer Methods in Applied Mechanics and Engineering Under review (2020) –.

[25] M. Arroyo, M. Ortiz, Local maximum-entropy approximation schemes: A seamless bridge between finite elements and meshfree methods, International Journal for Numerical Methods in Engineering 65 (13) (2006) 2167–2202. doi:10.1002/nme.1534.

[26] D. L. Sulsky, H. Schreyer, Z. Chen, A particle method for history-dependent materials, Computer Methods in Applied Mechanics and Engineering 118 (1) (1994) 179–196. doi:10.1016/0045-7825(94)90112-0.

[27] E. Jaynes, Information Theory and Statistical Mechanics, The Physical Review 106 (4) (1957) 620–630. doi:10.1103/PhysRev.106.620.

[28] C. E. Shannon, A Mathematical Theory of Communication, Bell System Technical Journal 27 (3) (1948) 379–423. doi:10.1002/j.1538-7305.1948.tb01338.x.

[29] P. Navas, R. Yu, G. Ruiz, Meshfree modeling of the dynamic mixed-mode fracture in frc through an eigensoftening approach, Engineering Structures 172 (2018) 94 – 104. doi:10.1016/j.engstruct.2018.06.010.

[30] M. P. Allen, D. J. Tildesley, Computer Simulation of Liquids, Clarendon Press, USA, 1989.

[31] S. G. S. G. Bardenhagen, E. M. Kober, The generalized interpolation material point method, CMES - Computer Modeling in Engineering and Sciences 5 (6) (2004) 477–495.

[32] I. Lim, I. Johnston, S. Choi, Stress intensity factors for semi-circular specimens under three-point bending, Engineering Fracture Mechanics 44 (3) (1993) 363 – 382. doi:10.1016/0013-7944(93)90030-V.

[33] X. Zhang, R. Yu, G. Ruiz, M. Tarifa, M. Camara, Effect of loading rate on crack velocities in hsc., International Journal of Impact Engineering 37 (2010) 359–370. doi:10.1016/j.ijimpeng.2009.10.002.

[34] S. Bardenhagen, J. Guilkey, K. Roessig, J. Brackbill, W. Witzel, J. Foster, An improved contact algorithm for the material point method and application to stress propagation in granular material, CMES. Computer Modeling in Engineering & Sciences 2 (4) (2001) 509–522. doi:10.3970/cmes.2001.002.509.

[35] P. Huang, X. Zhang, S. Ma, X. Huang, Contact algorithms for the material point method in impact and penetration simulation, International Journal for Numerical Methods in Engineering 85 (2011) 498 – 517. doi:10.1002/nme.2981.

[36] K. Wang, W. Sun, A unified variational eigen-erosion framework for interacting brittle fractures and compaction bands in fluid-infiltrating porous media, Computer Methods in Applied Mechanics & Engineering 318 (2017) 1 – 32. doi:10.1016/j.cma.2017.01.017.